ACS OMEGA

Article

Cite This: ACS Omega 2019, 4, 21962−21966

http://pubs.acs.org/journal/acsodf

Direct Near-Field Observation of Surface Plasmon Polaritons on Silver Nanowires

Matthias M. Wiecha,*[,†] Shihab Al-Daffaie,[‡] Andrey Bogdanov,[§] Mark D. Thomson,[†] Oktay Yilmazoglu,[‡] Franko Küppers,[∥] Amin Soltani,[†] and Hartmut G. Roskos[†]

[†]Physikalisches Institut, Goethe-Universität, Max-von-Laue Straße 1, D-60438 Frankfurt am Main, Germany

[‡]Institut für Mikrowellentechnik und Photonik, TU Darmstadt, Merckstraße 25, D-64283 Darmstadt, Germany

[§]Department of Nanophotonics and Metamaterials, ITMO University, St. Petersburg 197101, Russia

[∥]Skolkovo Institute of Science & Technology, Skolkovo Innovation Centre, Nobel Street 3, Moscow 121205, Russia

Supporting Information

ABSTRACT: Surface plasmon polaritons on (silver) nanowires are promising components for future photonic technologies. Here, we study near-field patterns on silver nanowires with a scattering-type scanning near-field optical microscope that enables the direct mapping of surface waves. We analyze the spatial pattern of the plasmon signatures for different excitation geometries and polarization and observe a plasmon wave pattern that is canted relative to the nanowire axis, which we show is due to a superposition of two different plasmon modes, as supported by electromagnetic simulations including the influence of the substrate. These findings yield new insights into the excitation and propagation of plasmon polaritons for applications in nanoplasmonic devices.

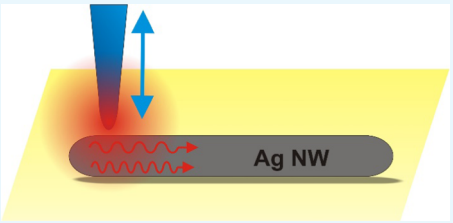

1. INTRODUCTION

Silver nanowires (Ag-NWs) have attracted a great deal of attention over the last few years. Due to their ability to carry subwavelength plasmon modes,[1,2] they are promising tools for future optoelectronic and nanophotonic applications, which aim at benefiting from the advantages of light (e.g., its speed) in photonic on-chip devices.[3−6] Recently, terahertz (THz) photomixers equipped with Ag NWs in their active region have shown an enhanced emission especially at higher frequencies (>1 THz) compared to the state-of-the-art interdigital photomixer design.[7] The incorporation of Ag NWs into photomixers leads to a significant reduction of the device capacitance of around 1 order of magnitude and increases the photocurrent by up to 32 times as compared to conventional photomixers. In such devices, it is still an open question whether plasmonic effects in the Ag NW also play an essential role in the device behavior, which is one motivation of the present study, investigating plasmons on Ag NWs excited by near-infrared light.

Surface plasmon polaritons (SPPs) on NWs, which support a set of various SPP modes, can be mapped and analyzed with various experimental techniques. The contribution of different plasmon modes has been investigated in the far field by quantum-dot fluorescence,[4,8] whereas near-field measurements by means of scanning near-field optical microscopy (SNOM)[9] just reported a single mode so far (all of these reports were in the optical range for Ag NWs). The scattering-type SNOM (s-SNOM) technique until now has been applied only in the infrared range e.g., on InAs NWs.[10]

Here, the s-SNOM technique is not only employed to map the near-field pattern of a single mode like in many other s-SNOM applications[11,12] but also to study different modes propagating simultaneously on Ag NWs. They are excited with near-infrared radiation at a wavelength of 853 nm, which is the frequency regime of the optical beat note of the respective THz photomixers employing nanowire contacts. The near-infrared s-SNOM measurements described in our paper focus on the question whether plasma waves are excited on a NW, even if its geometry has not been optimized or specifically selected to support resonances of such waves. How effectively such plasma waves contribute to the efficiency of the photomixers will be the subject of future studies.

Free-standing NWs possess cylindrical symmetry and one can readily solve Maxwell's equations to find the dispersion and field distributions[8,13−15] for each plasmon mode. For the case here, where the NW lies on a substrate, one must solve for the modes numerically,[4,16,17] which leads to a similar set of modes, only with modified dispersion and asymmetric field distributions. We also simulate the plasmon modes for our specific case here.

Typically s-SNOM measurements employ p-polarized incident light, i.e., where the incident electric field has a component parallel to the atomic force microscope (AFM) tip (see Figure 1a), which can then act as an antenna.[18] However, for p-polarized light, we observe only plasmons on the Ag NW

Received: September 17, 2019
Accepted: November 19, 2019
Published: December 13, 2019

DOI: 10.1021/acsomega.9b03036
ACS Omega 2019, 4, 21962−21966

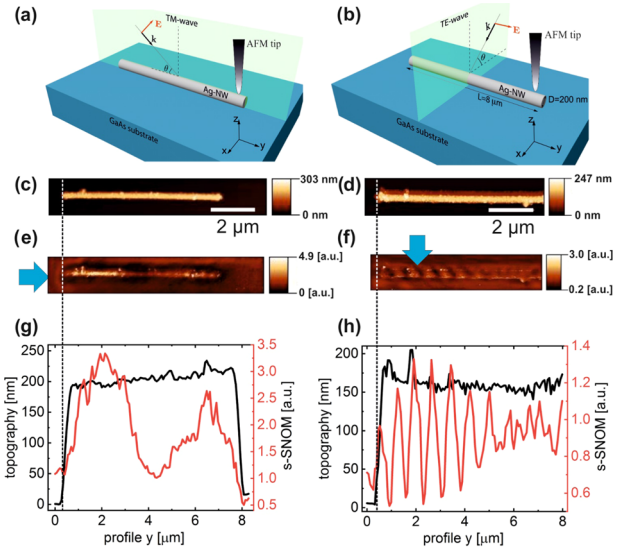

Figure 1. s-SNOM signals and associated results for SPPs on a 200 nm diameter Ag NW, for both p- (left column) and s-polarization (right column). (a, b) Schematic of field geometries: for p-polarization, the incident *k*-vector is within the *yz*-plane (at an angle θ ~30° to the substrate) with the E-field in the *yz*-plane, while for s-polarization, the incident *k*-vector is within the *xz*-plane (again with θ ~30°) and the E-field along the *y*-axis. (c, d) AFM topography of the nanowire recorded in parallel to each 2Ω s-SNOM image measurements shown in (e, f). The blue arrows indicate the incident laser direction. (g, h) Averaged lineouts of the image data in (c–f) extracted along the central axis of the NW.

if it is oriented parallel to the incident direction, i.e., a portion of the E-field is parallel to the NW as well. An ~90°-rotated NW shows no plasmon response at all (see the Supporting Information; Figure S2). Additionally, we also performed s-SNOM measurements with s-polarized excitation, which allows one to have the incident field purely along the NW axis (using a proper sample alignment). In both cases, the orientation of the NW axis was chosen to have the maximum incident field component along the NW axis (by rotating the sample plane, see Figure 1b) and the polarization of the external local-oscillator beam (used for heterodyne detection of the scattered light collected from the tip and delivered to the photodetector) was rotated to measure mainly the *z*-component (i.e., perpendicular to the sample plane) of the surface-wave electric field.[19] The incident beam angle was ~30° for all measurements.

2. RESULTS AND DISCUSSION

Figure 1a,b shows the schematics of the p- and s-polarization geometries, respectively, while the corresponding AFM images of the NW are presented in Figure 1c,d. The simultaneous second-harmonic (2Ω) pseudo-heterodyne[20] s-SNOM measurements are presented in Figure 1e,f for p- and s-polarization, respectively. Figure 1g,h shows the respective lineouts along the central axis of the NW from these near-field images. In both p- and s-polarized cases, there is a clearly observable signal measured along the wire, which contains a contribution from the SPPs. The third-harmonic (3Ω) s-SNOM data (Figure S3a,b), which offer higher background suppression, reproduces the 2Ω signal pattern in Figure 1. However, due to the lower signal-to-noise ratio for 3Ω-detection, we concentrate on the 2Ω s-SNOM data for the subsequent analysis. The optical phase (measured in parallel to Figure 1f by the interferometric detection) supports our findings (Figure S3c,d). Both measurements in Figure 1 are on the same NW. The doubled "ghost" image in Figure 1d is due to a double tip (the same tip as in Figure S2). However, simple geometrical considerations (to exclude that the tilted pattern is a "double" image) as well as the reproduction of the pattern in further measurements (amongst others Figure S6) convinced us that it is justifiable to choose the measurement with the highest signal-to-noise ratio for quantitative analysis since only the averaged lineouts along the NWs are taken into account.

In contrast to previous reports in the mid-IR, where SPPs are launched by the tip and form standing waves due to reflections from both ends of the structures (for NWs[10] and other structures[12]), here the surface modes are launched due to scattering at the NW end facets, which is known for optical/NIR frequency experiments.[21]

In the p-polarization measurement, the SPPs are launched by the NW facet oriented toward the incident light (left column, Figure 1e). In addition to the surface waves, a second signal contribution E_m is produced directly at the tip, i.e., due to the conventional s-SNOM dielectric contrast signal.[22] As expected in the near-infrared, the latter signal is stronger in the image above the Ag NW than the substrate. The crucial point that determines the form of the interference is the phase difference ΔΦ between the SPP waves (which propagate along the NW with wavevector k_{spp}) compared to the material contribution (where the beam propagates directly to the tip with an in-plane wavevector component $k_0 \cdot \cos\theta$) at the position of the tip, where the SPP is coupled out into far-field radiation. The two waves (SPP and material scattered field) form an interference pattern with a wavelength Λ that is mapped by s-SNOM. The straightforward geometrical considerations depicted in Figure 2a yield eqs 1 and 2, for the phase shift and wavelength of the interference between SPP and conventional s-SNOM signals

$$\Delta\Phi = (k_{spp} - k_0\cos\theta)(y - y_1) \quad (1)$$

$$\Lambda = \frac{2\pi}{k_{spp} - k_0\cos\theta} \quad (2)$$

While we present a quantitative modeling of the expected signal vs position along the NW axis below, one sees immediately from eq 2 that for $k_{spp} \approx k_0\cos\theta$, a long-wave interference pattern ($\Lambda \gg \lambda_{spp},\lambda_0$) is expected (e.g., a mode with λ_{SPP} = 852 nm, λ_0 = 853 nm, and θ = 30° is observed with a wavelength of Λ ~6.3 μm).

Another intriguing aspect of the p-polarization model is that only excitation from the end facet closer to the incident laser is required to explain the measurement. An excitation from the other side would result in a plus sign in the denominator of eq 2, and therefore, an additional wave pattern $\Lambda < \lambda_0$ close to the right end should be visible but have not been observed. This could be explained since both sides are not symmetrical, and indeed, the excitation geometry differs;[23] on the incident side of the NW, the charges can be separated more easily (see Figure S4). This is confirmed as well by additional measurements with a 180° rotation of the nanowire (see Figure S5), where a similar pattern is observed. Since the laser spot is focused on the tip and the sample is scanned beneath, the launching of SPPs at the edge gets weaker with a Gaussian dependence with increasing *y* as the tip and input beam center

DOI: 10.1021/acsomega.9b03036
ACS Omega 2019, 4, 21962−21966

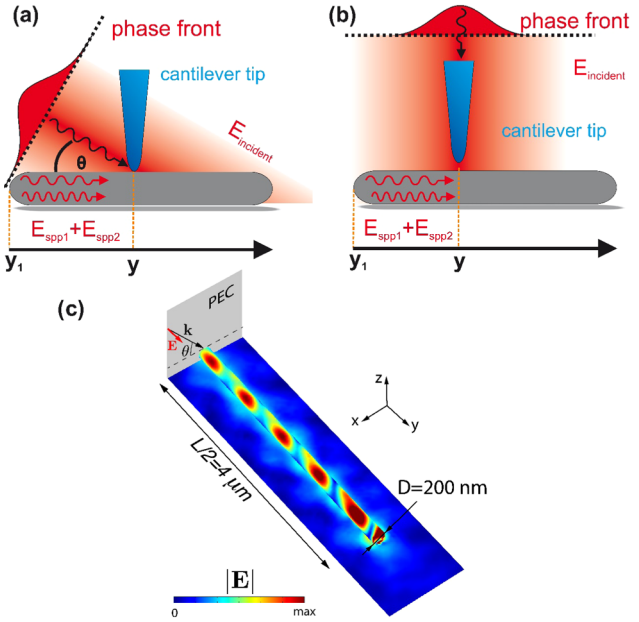

Figure 2. Sketches of the models to explain the experimental data for (a) p-polarization and (b) s-polarization. (c) Distribution of the electric field amplitude calculated in COMSOL Multiphysics for s-polarization. The geometry of the problem and TE-polarization of the incident wave allow the reduction of the model using a perfect electrical conductor (PEC) boundary condition at the plane perpendicular to the wire crossing its center.

move away from the edge (see Figure 2a,b). This effect is dominant in comparison to the signal decay due to SPP propagation loss. For this reason and also considering the wire length, the reflection of the SPP at the opposite end of the NW is not considered to form a Fabry–Perot resonator as in other studies.[9,24]

The p-polarization configuration will be later fitted with two modes (the explanation of the two modes' properties follows in the next paragraph about the s-polarization; we interpret both measurements with the same two modes) and one could in principle interpret and fit the p-polarization data with a single mode as well. However, as already stated in eq 1 due to the phase retardation effect by the E_m-field, the observed SPP wavelength results in a much higher interference wavelength Λ (see eq 2), and therefore, two modes are barely distinguishable in this measurement since Λ is larger than the entire fitting range due to the Gaussian beam shape.

The degradation in the s-SNOM signal directly behind the NW (at ∼8 μm in Figure 1g) can be explained by a shadowing effect of the NW itself (taking note of the incident direction from the left).

With the incident s-polarized light, there is neither a material contribution excited in the s-SNOM since there is no field component parallel to the tip (indeed in the experiment, the components are always at least slightly present and coupled) or any phase shift of the field at the end of the NW where the SPPs are excited (see Figure 2b). For this measurement, higher laser power and lock-in time constants (100 ms instead of 20 ms for p-polarization) are used to obtain a satisfactory data quality. One way to interpret this geometry is to consider eq 2 with θ = 90°, which corresponds to a constant phase shift between the SPP waves and material contribution, such that one measures the SPP wavelengths directly. The increase in the signal envelope in the first few microns (cf. Figure 1f for y in the range between 0 and 2 μm) is already suggestive of beating between more than one SPP mode, which is also implied by the tilted spatial pattern (Figure 1f). A similar pattern was reported in the case of NWs in a homogeneous environment, where the fundamental mode (TM_0) together with a phase-shifted higher-order mode can form chiral and tilted patterns[4] (the phase shift of the latter was due to the specific excitation geometry). Since there are similar mode shapes in the case of Ag NW on substrates,[4,17] we deduce that this behavior is present as well in our case, as supported by the simulations below. The theory of the different modes is described in detail in ref 4. However, the applied experimental technique of quantum-dot fluorescence imaging has a limited spatial resolution and is only capable of detecting the far-field beating pattern of the intensity, whereas our s-SNOM measurements reveal the full electric field distribution with subwavelength resolution and therefore complement those studies.

For the s-polarization measurement, we also attribute the asymmetric SPP pattern to an asymmetric excitation of the two nanowire ends (Figure S4) to explain why only SPPs launched from one side are dominant in the data. Since the samples are positioned by hand, there is always a slight deviation from the ideal 90° angle between incident light and the NW axis. In additional control measurements with a different fine tuning of the NW orientation relative to the input beam, one can also achieve the situation where the dominant SPP signals originate from the opposite end (see the Supporting Information; Figure S6).

To obtain the SPP wavelengths and to verify our interpretation, additional numerical simulations were performed using COMSOL Multiphysics (for details, see the Supporting Information). Two leaky eigenmodes (with k_{y1} = $0.993k_0$ and k_{y2} = $1.001k_0$, respectively) can be identified for the Ag NW on the GaAs substrate system (see Figure S7) for an incident wavelength of 853 nm, in addition to a third eigenmode, which is not detectable by our s-SNOM measurements because its field is nearly entirely concentrated in the substrate beneath the NW and will therefore not be considered further in the data analysis. The intensity of the total field of both modes is presented in Figure 2c. The data support that an excitation of the NW end can result in the tilted field distribution seen experimentally (Figure 1f). Using the two eigenmode wavelengths and our models (Figure 2a,b), the averaged near-field lineouts (cf. Figure 1g,h) can be fitted well, as shown in Figure 3a,b. For the p-polarization measurement, two propagating and phase-retarded modes (see eq 1) are considered together with a dielectric material offset term, whereas in the s-polarization measurement, the two modes are mapped directly (with an arbitrary offset instead of the material term). Although the propagation length of the modes are taken into account, the decreasing behavior in both measurements is dominated by the Gaussian beam shape of the excitation spot (see Figure 2a,b). The decomposition of the simulation in Figure 3a,b (blue curve) into its different components is shown in Figure 3c,d.

In the p-polarization case, one mode amplitude is ∼20 times higher, and therefore, mainly this mode is excited. However, in the s-polarization measurement, both amplitudes are quite similar (7% deviation). The explicit equations and the fitting procedure are described further in the Supporting Information. To support our findings, the p-polarization measurement was repeated as well on another NW with a λ_0 = 780 nm laser; the

DOI: 10.1021/acsomega.9b03036
ACS Omega 2019, 4, 21962−21966

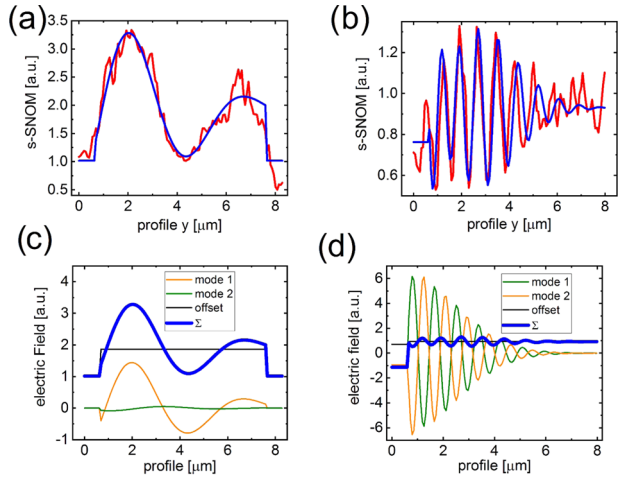

Figure 3. Measured s-SNOM signals (red) and corresponding fits (blue) based on the models in Figure 2a,b for (a) p-polarization and (b) s-polarization. (c, d) Two different modes and a constant background term contribute to the simulated signal (blue), respectively.

shorter resulting SPP wavelength is confirmed by three visible maxima (Figure S8).

We close by considering whether the NW may support plasmon resonances in its transverse direction. Such resonances should be excited efficiently if the incident light is polarized in the transverse direction of the NW. However, we did not observe corresponding resonance signatures in our s-SNOM measurements for this case (see Figure S2). In fact, the two modes which are accessible to the s-SNOM measurements have wavelengths of 852 and 859 nm (see Figure S7), too large to allow formation of a standing wave on the 200 nm-wide wire.[25−27] The "hidden" mode of Figure S7 (propagating nearly entirely in the substrate) is expected to have a wavelength of 233 nm and may become resonant. As we cannot determine from our NIR s-SNOM measurements whether this is the case, one should refer to measurements on full photomixer devices. The efficiency of the THz-generation process should depend on the polarization of the incident NIR laser light. Unfortunately, such measurements have not been reported yet.

3. CONCLUSIONS

In summary, we have mapped out the field patterns of surface plasmon polaritons on a silver nanowire in an inhomogeneous environment (wires on GaAs, exposed to air). The polaritons have been generated by near-infrared excitation and probed using the near-field capabilities of an s-SNOM microscope. We have observed a single mode for p-polarized excitation and a tilted dual-mode pattern in the case of s-polarization. We can account for the signal profiles of both cases using a propagation model for plasmon polaritons, whose wavelengths have been derived from electromagnetic simulations. The model considers the interference between signal contributions as well as the excitation beam profile. To improve the understanding of the efficiency enhancement of THz photomixers that employ such Ag nanowires as electrical contacts, the next step will be to apply nanoscopic detection methods to map the THz near-fields close to the nanowires in a photomixer device driven by two-color near-infrared excitation and to test whether one finds an enhanced density of excited charge carriers in the close vicinity of the wire.

4. EXPERIMENTAL SECTION

The s-SNOM technique employs a near-field microscope based on an atomic force microscope (AFM) in noncontact mode. A laser is focused on the tip−sample region and due to a near-field interaction, a portion of the light is scattered away that contains information about the dielectric properties of the sample beneath the tip. The spatial resolution is not limited by the focal beam diameter but rather by the lateral dimensions of the tip (typically ∼20 nm), which is independent of the wavelength used.[18] The measured signals are demodulated at higher harmonics of the cantilever tapping frequency Ω to suppress background signal contributions in combination with an interferometric pseudo-heterodyne detection scheme.[18,20] Topographical AFM images and near-field s-SNOM images are always recorded simultaneously. Another powerful application of the s-SNOM platform besides nanoimaging of the surface dielectric properties is the mapping of surface electromagnetic waves, which can be excited by the incident light and subsequently converted back to scattered waves by the tip after propagation along the surface. Interference of the surface-wave signals and directly scattered fields leads to the formation of standing wave patterns that are manifested in the s-SNOM images.[12,28] However, one must take care to correctly identify and interpret the different contributions (and their interference), especially in the optical/NIR regime.[21,29] The details of the s-SNOM apparatus employed here are given in the Supporting Information. The considered sample consists of Ag-NWs from ACS Material arranged manually on a 1 μm-thick layer of low-temperature-grown (LTG)-GaAs (grown on a 350 μm-thick undoped GaAs substrate; Wafer Technology Ltd.), which is also used for THz nano-photomixers (see the Supporting Information; Figure S1).

■ ASSOCIATED CONTENT

Supporting Information

The Supporting Information is available free of charge at https://pubs.acs.org/doi/10.1021/acsomega.9b03036.

Details about the experimental setup, simulations, and fitting procedure; additional measurements and figures (PDF)

■ AUTHOR INFORMATION

Corresponding Author

*E-mail: wiecha@physik.uni-frankfurt.de.

ORCID

Matthias M. Wiecha: 0000-0002-4485-1822

Amin Soltani: 0000-0002-3701-9528

Author Contributions

The manuscript was written through contributions of all authors. S.A.-D. prepared and provided the samples. M.M.W. performed the measurements and the data analysis. A.S. and A.B. were responsible for the simulations. All authors have given approval to the final version of the manuscript.

Notes

The authors declare no competing financial interest.

DOI: 10.1021/acsomega.9b03036
ACS Omega 2019, 4, 21962−21966

■ ACKNOWLEDGMENTS

A.B. acknowledges support by the Ministry of Education and Science of the Russian Federation (3.1668.2017/4.6; 3.8891.2017/8.9) and RFBR (18-29-20063; 17-02-01234). M.M.W. acknowledges the Adolf Messer Stiftung for funding his doctoral studies.

■ ABBREVIATIONS

AFM, atomic force microscope; NIR, near-infrared; NW, nanowire; s-SNOM, scattering-type scanning near-field optical microscopy; THz, terahertz

■ REFERENCES

(1) Jones, A. C.; Olmon, R. L.; Skrabalak, S. E.; Wiley, B. J.; Xia, Y. N.; Raschke, M. B. Mid-IR Plasmonics: Near-Field Imaging of Coherent Plasmon Modes of Silver Nanowires. *Nano Lett.* **2009**, *9*, 2553−2558.

(2) Sanders, A. W.; Routenberg, D. A.; Wiley, B. J.; Xia, Y.; Dufresne, E. R.; Reed, M. A. Observation of Plasmon Propagation, Redirection, and Fan-out in Silver Nanowires. *Nano Lett.* **2006**, *6*, 1822−1826.

(3) Wei, H.; Pan, D.; Zhang, S.; Li, Z.; Li, Q.; Liu, N.; Wang, W.; Xu, H. Plasmon Waveguiding in Nanowires. *Chem. Rev.* **2018**, *118*, 2882−2926.

(4) Wei, H.; Pan, D.; Xu, H. Routing of Surface Plasmons in Silver Nanowire Networks Controlled by Polarization and Coating. *Nanoscale* **2015**, *7*, 19053−19059.

(5) Fang, Y.; Sun, M. Nanoplasmonic Waveguides: Towards Applications in Integrated Nanophotonic Circuits. *Light: Sci. Appl.* **2015**, *4*, No. e294.

(6) Wei, H.; Li, Z. P.; Tian, X. R.; Wang, Z. X.; Cong, F. Z.; Liu, N.; Zhang, S. P.; Nordlander, P.; Halas, N. J.; Xu, H. X. Quantum Dot-Based Local Field Imaging Reveals Plasmon-Based Interferometric Logic in Silver Nanowire Networks. *Nano Lett.* **2011**, *11*, 471−475.

(7) Al-Daffaie, S.; Yilmazoglu, O.; Küppers, F.; Hartnagel, H. L. 1-D and 2-D Nanocontacts for Reliable and Efficient Terahertz Photomixers. *IEEE Trans. Terahertz Sci. Technol.* **2015**, *5*, 398−405.

(8) Zhang, S.; Wei, H.; Bao, K.; Håkanson, U.; Halas, N. J.; Nordlander, P.; Xu, H. Chiral Surface Plasmon Polaritons on Metallic Nanowires. *Phys. Rev. Lett.* **2011**, *107*, No. 096801.

(9) Ditlbacher, H.; Hohenau, A.; Wagner, D.; Kreibig, U.; Rogers, M.; Hofer, F.; Aussenegg, F. R.; Krenn, J. R. Silver Nanowires as Surface Plasmon Resonators. *Phys. Rev. Lett.* **2005**, *95*, No. 257403.

(10) Zhou, Y.; Chen, R.; Wang, J.; Huang, Y.; Li, M.; Xing, Y.; Duan, J.; Chen, J.; Farrell, J. D.; Xu, H. Q.; et al. Tunable Low Loss 1D Surface Plasmons in InAs Nanowires. *Adv. Mater.* **2018**, *30*, No. 1802551.

(11) Yoxall, E.; Schnell, M.; Nikitin, A. Y.; Txoperena, O.; Woessner, A.; Lundeberg, M. B.; Casanova, F.; Hueso, L. E.; Koppens, F. H. L.; Hillenbrand, R. Direct Observation of Ultraslow Hyperbolic Polariton Propagation with Negative Phase Velocity. *Nat. Photonics* **2015**, *9*, 674.

(12) Fei, Z.; Rodin, A. S.; Andreev, G. O.; Bao, W.; McLeod, A. S.; Wagner, M.; Zhang, L. M.; Zhao, Z.; Thiemens, M.; Dominguez, G.; et al. Gate-Tuning of Graphene Plasmons Revealed by Infrared Nano-Imaging. *Nature* **2012**, *487*, 82−85.

(13) Chang, D. E.; Sørensen, A. S.; Hemmer, P. R.; Lukin, M. D. Strong Coupling of Single Emitters to Surface Plasmons. *Phys. Rev. B* **2007**, *76*, No. 035420.

(14) Pfeiffer, C. A.; Economou, E. N.; Ngai, K. L. Surface Polaritons in a Circularly Cylindrical Interface: Surface Plasmons. *Phys. Rev. B* **1974**, *10*, No. 3038.

(15) Spittel, R.; Uebel, P.; Bartelt, H.; Schmidt, M. A. Curvature-Induced Geometric Momenta: The Origin of Waveguide Dispersion of Surface Plasmons on Metallic Wires. *Opt. Express* **2015**, *23*, No. 12174.

(16) Zhang, S.; Xu, H. Optimizing Substrate-Mediated Plasmon Coupling toward High-Performance Plasmonic Nanowire Waveguides. *ACS Nano* **2012**, *6*, 8128−8135.

(17) Jia, Z.; Wei, H.; Pan, D.; Xu, H. Direction-Resolved Radiation from Polarization-Controlled Surface Plasmon Modes on Silver Nanowire Antennas. *Nanoscale* **2016**, *8*, 20118−20124.

(18) Keilmann, F.; Hillenbrand, R. Near-Field Microscopy by Elastic Light Scattering from a Tip. *Philos. Trans. R. Soc., A* **2004**, *362*, 787−805.

(19) Huber, A. J.; Crozier, K.; Aizpurua, J.; Hillenbrand, R. Controlling the Near-Field Oscillations of Loaded Plasmonic Nanoantennas. *Nat. Photonics* **2009**, *3*, 287−291.

(20) Ocelic, N.; Huber, A.; Hillenbrand, R. Pseudoheterodyne Detection for Background-Free near-Field Spectroscopy. *Appl. Phys. Lett.* **2006**, *89*, No. 101124.

(21) Li, Y.; Zhou, N.; Kinzel, E. C.; Ren, X.; Xu, X. The Origin of Interferometric Effect Involving Surface Plasmon Polariton in Scattering Near-Field Scanning Optical Microscopy. *Opt. Express* **2014**, *22*, No. 2965.

(22) Keilmann, F.; Taubner, T.; Hillenbrand, R. Performance of Visible and Mid-Infrared Scattering-Type near-Field Optical Microscopes. *J. Microsc.* **2003**, *210*, 311−314.

(23) Wang, B.; Aigouy, L.; Bourhis, E.; Gierak, J.; Hugonin, J. P.; Lalanne, P. Efficient Generation of Surface Plasmon by Single-Nanoslit Illumination under Highly Oblique Incidence. *Appl. Phys. Lett.* **2009**, *94*, No. 011114.

(24) Rossouw, D.; Couillard, M.; Vickery, J.; Kumacheva, E.; Botton, G. A. Multipolar Plasmonic Resonances in Silver Nanowire Antennas Imaged with a Subnanometer Electron Probe. *Nano Lett.* **2011**, *11*, 1499−1504.

(25) Rossouw, D.; Botton, G. A. Plasmonic Response of Bent Silver Nanowires for Nanophotonic Subwavelength Waveguiding. *Phys. Rev. Lett.* **2013**, *110*, No. 066801.

(26) Mock, J. J.; Oldenburg, S. J.; Smith, D. R.; Schultz, D. A.; Schultz, S. Composite Plasmon Resonant Nanowires. *Nano Lett.* **2002**, *2*, 465−469.

(27) Rothe, M.; Zhao, Y.; Kewes, G.; Kochovski, Z.; Sigle, W.; van Aken, P. A.; Koch, C.; Ballauff, M.; Lu, Y.; Benson, O. Silver Nanowires with Optimized Silica Coating as Versatile Plasmonic Resonators. *Sci. Rep.* **2019**, *9*, No. 3859.

(28) Huber, A.; Ocelic, N.; Kazantsev, D.; Hillenbrand, R. Near-Field Imaging of Mid-Infrared Surface Phonon Polariton Propagation. *Appl. Phys. Lett.* **2005**, *87*, No. 081103.

(29) Walla, F.; Wiecha, M. M.; Mecklenbeck, N.; Beldi, S.; Keilmann, F.; Thomson, M. D.; Roskos, H. G. Anisotropic Excitation of Surface Plasmon Polaritons on a Metal Film by a Scattering-Type Scanning near-Field Microscope with a Non-Rotationally-Symmetric Probe Tip. *Nanophotonics* **2018**, *7*, 269−276.

DOI: 10.1021/acsomega.9b03036
ACS Omega 2019, 4, 21962−21966